Bioorganic Chemistry 183 (2026) 110637



Contents lists available at ScienceDirect

Bioorganic Chemistry

journal homepage: www.elsevier.com/locate/bioorg





Phormidolide D, a novel cytotoxic cyanobacterial macrolide: Assessing its effects on the extracellular matrix, apoptosis, and angiogenesis☆

Leonor Ferreira [a,b], Tiago Ribeiro [a,1], Ravindra Peravali [c], Vítor Vasconcelos [a,b], Ralph Urbatzka [a], Mariana Reis [a,*]

[a] CIIMAR/CIMAR LA, Interdisciplinary Centre of Marine and Environmental Research, University of Porto, Terminal de Cruzeiros do Porto de Leixões, Matosinhos, 4450-208, Portugal

[b] Faculty of Sciences, University of Porto (FCUP), Rua do Campo Alegre, Porto, 4169-007, Portugal

[c] Institute of Toxicology and Genetics (ITG), Karlsruhe Institute of Technology (KIT), Hermann-von-Helmholtz-Platz 1, Eggenstein-Leopoldshafen, 76344, Germany

ARTICLE INFO

Keywords:
Marine cyanobacteria
Halogenated polyketide
Colorectal cancer
3D spheroids
Extracellular matrix
Zebrafish
Anti-angiogenesis

ABSTRACT

Marine cyanobacteria are a rich source of structurally diverse secondary metabolites and have inspired at least four anticancer drugs currently on the market, highlighting their potential for the discovery of new therapeutic candidates. This study aimed to discover and elucidate the structure of a novel halogenated polyketide from marine cyanobacteria and to characterize its cytotoxic and mechanistic profile.

Phormidolide D (**1**) was discovered through bioactivity-guided isolation, and its structure was elucidated using NMR and HR-MS/MS analyses. Cytotoxicity was evaluated in SH-SY5Y, HepG2, HCT 116, and hCMEC/D3 cell lines. Its biological activity was further characterized in 2D and 3D HCT 116 models by assessing spheroid morphology, extracellular matrix-related mRNA expression, combination effects with staurosporine, cell cycle distribution and apoptosis. In vivo anti-angiogenic activity was evaluated in transgenic zebrafish (Tg(*fli1a*:EGFP) embryos. Phormidolide D (**1**) exhibited potent cytotoxicity against the human colon carcinoma cell line HCT 116 in both monolayer and spheroid cultures (IC_{50} = 0.83 μM and 30.80 μM, respectively), whereas phormidolide A (**2**) was inactive. Phormidolide D (**1**) affected the 3D spheroid architecture, as demonstrated by fluorescence imaging. Its effects on the extracellular matrix were further observed by increased matrix metalloproteinase 1 mRNA expression and reduced collagen type I transcripts. Co-treatment of a phormidolide rich fraction with sub-effective concentrations of staurosporine reduced spheroid viability, with Bliss analysis confirming a synergistic interaction. Treatment with phormidolide D (**1**) increased sub-G1 cell population and early apoptotic cells. Furthermore, transgenic zebrafish embryos exposed to phormidolide D (**1**) had reduced vascularization, suggesting further studies for anti-angiogenic potential.

These findings highlight phormidolide D (**1**), a structurally unique marine natural product distinguished by an unprecedented bromomethylene ketone, as a promising lead for anticancer drug development.

1. Introduction

Over the last century, understanding of cancer biology and therapeutics has evolved significantly. Despite this, cancer remains the second leading cause of death worldwide among non-communicable diseases, with lung, colorectal, and liver cancers being the deadliest [1]. The International Agency for Research on Cancer (IARC) predicts a 77% increase in new cancer cases from 2022 to 2050, placing strain on healthcare systems [2]. While current oncological treatments have improved patient outcomes, challenges such as therapeutic resistance, systemic toxicity, and tumor heterogeneity necessitate the continued development of innovative anticancer agents [1].

Therapeutic strategies targeting cell cycle arrest and apoptosis induction have long been central to oncological treatment, as cancer is characterized by uncontrolled cell proliferation. However, cancer progression also involves local tissue invasion and distant metastatic

☆ This article is part of a Special issue entitled: 'Marine natural products' published in Bioorganic Chemistry.

* Corresponding author.
E-mail address: mreis@ciimar.up.pt (M. Reis).

[1] +Present address: Fish Immunology and Vaccinology, Instituto de Investigação e Inovação em Saúde (i3S), Universidade do Porto, Rua Alfredo Allen 208, 4200–135 Porto, Portugal.

https://doi.org/10.1016/j.bioorg.2026.110637
Received 28 August 2026; Received in revised form 30 September 2026; Accepted 8 October 2026
Available online 12 October 2026
0045-2068/© 2026 The Author(s). Published by Elsevier Inc. This is an open access article under the CC BY license (http://creativecommons.org/licenses/by/4.0/).

spread, processes that rely on the tumor microenvironment and its major component, the extracellular matrix (ECM) [3]. The ECM is a complex three-dimensional network of macromolecules such as collagens and fibronectin, that provides structure and support to cells while regulating diverse cellular functions [4]. Abnormal ECM remodeling can promote cell growth, invasion, and metastasis, while its dense architecture reduces drug delivery and fosters chemoresistance, making it a compelling target for therapeutic intervention [3].

Closely linked to ECM dynamics, angiogenesis relies on ECM-derived structural support and biochemical signaling for the development of new blood vessels [5]. Since tumors depend on angiogenesis for oxygen and nutrient supply, and aberrant vessel formation sustains tumor growth and facilitates metastatic dissemination, inhibiting this process has emerged as a key therapeutic strategy [6].

In this context, natural products have played an essential role in cancer drug discovery due to their chemical diversity and multitarget activity [7]. Among marine microbial sources, cyanobacteria are particularly rich in secondary metabolites, including peptides, polyketides, and hybrid peptide–polyketide compounds [8]. These ubiquitous photosynthetic prokaryotes produced highly potent bioactive compounds, most notably dolastatin 10, whose pharmacophore served as the basis for clinically approved anticancer drugs currently used in oncology [9].

The phormidolide family, featuring a tetrahydrofuran ring in their macrolactone core, represents an intriguing class with structure-dependent bioactivity profiles. Phormidolide A (**2**), first isolated in 2002 [10] from the cyanobacterium *Leptothoe* sp. ISB3NOV94-8 A [11], bears a 16-membered lactone ring connected to a polyhydroxylated chain, bearing a palmitic ester residue and terminating in a bromomethoxydiene, and has since been the subject of studies aimed at elucidating its absolute configuration [12], [13] and total synthesis [14], [15]. Despite this chemical interest, phormidolide A (**2**) was inactive against the NCI-60 human cancer cell line panel [10]. In contrast, phormidolides B and C, isolated from a marine sponge belonging to the Petrosiidae family, show strong cytotoxicity against three human tumor cell lines, differing structurally by a 14-membered lactone and a halogenated fatty acyl chain [14]. These opposing bioactivity profiles highlight how structural variations critically influence the pharmacological properties within this family.

Here, we report the isolation and structure elucidation of phormidolide D (**1**) (Fig. 1), a new member of the phormidolide family from the marine cyanobacterium *Leptothoe* sp. LEGE 181152 collected in São Vicente Island, Cabo Verde. Its biological activity was evaluated through complementary in vitro and in vivo models to evaluate its cytotoxicity, ECM and anti-angiogenic outcomes, as well as combinatory effects with staurosporine. This work aimed to provide a mechanistic characterization of phormidolide D (**1**) as a basis for its further development as a promising anticancer lead.

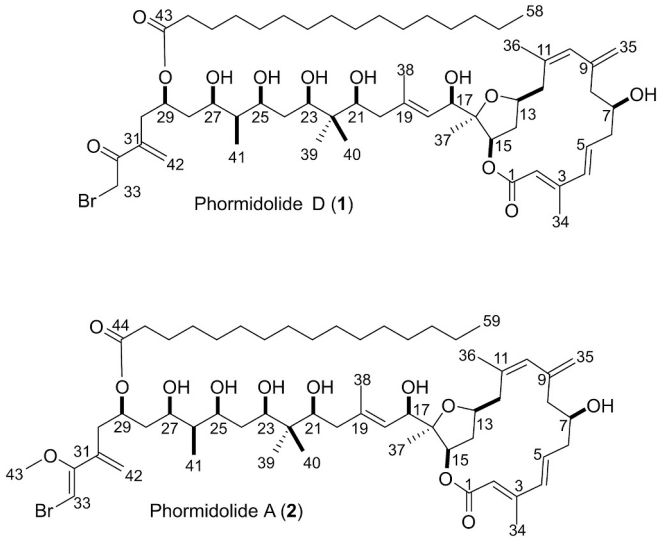


Fig. 1. Structures of phormidolide D (**1**) and phormidolide A (**2**).

2. Materials and methods

2.1. General chemical procedures

All information regarding general chemical procedures and the materials used can be found in supplementary material.

2.2. Biomass production and isolation of phormidolides from Leptothoe sp. 181,152, and annotation of its biosynthetic gene cluster (BGC)

The marine cyanobacterial strain *Leptothoe* sp. LEGE 181152, described by Avalon et al., 2024 [11] and deposited in the Blue Biotechnology and Ecotoxicology Culture Collection (LEGE-CC), was grown using Z8 medium supplemented with 25‰ of synthetic sea salt (Tropic Marin® Pro-Reef, Tropic Marin, Berlin, Germany) and 1‰ of vitamin B_{12}. Cultures were scaled up to 20 L and maintained under standard laboratory conditions: 25 °C with a light/dark cycle of 14/10 h at a light intensity of 10–30 μmol photons m^{-2} s^{-1}. At the end of the exponential phase, cells were harvested by filtration through a 20 μm mesh, frozen and freeze-dried (LyoQuest, Telstar, Terrassa, Spain), yielding 80 g of biomass. The lyophilized biomass was extracted with MeOH and sonication at room temperature. The resulting crude (28.5 g) was fractionated in several chromatographic rounds yielding 1.5 mg of pure phormidolide D (**1**) and 1.14 mg of pure phormidolide A (**2**). A detailed description of the isolation process as well as annotation of the BGC can be found in the supplementary material.

2.3. Cell lines and culture

HCT 116 Human colon carcinoma cell line was cultured in McCoy's media, SH-SY5Y neuroblastoma cells were cultured in 1:1 Minimum Essential Medium (MEM) and F12 medium and hepatocellular carcinoma HepG2 and endothelial hCEMEC/D3 cell lines were cultured in DMEM. All media were supplemented with 10% Fetal Bovine Serum (FBS), 1% penicillin/streptomycin and 0.1% of amphotericin B. Cells were maintained at 37 °C in a humidified atmosphere of 5% CO2. For the glucose versus galactose assay, HCT 116 cells were cultured in glucose-containing or glucose-free McCoy's 5 A medium, supplemented as described above.

2.4. Cell viability assays on monolayer cell cultures

All cell lines were seeded on 96-well plates at a density of 3.3×10^4 cells/mL and incubated overnight to allow adhesion. For the MTT assay, cells were exposed to compounds at a concentration range up to 40 μM, with staurosporine (500 nM) as positive control. After 48 h, cell viability was assessed using the MTT (3-(4,5- dimethylthiazol-2-yl)-2,5-diphenyltetrazolium bromide) assay, as previously described [16]. For the lactate dehydrogenase (LDH) release assay, cells were treated under the same conditions. After 48 h, 50 μL of culture supernatant from treated cells (phormidolide D (**1**) or Triton X-100 at 1%, positive control) were transferred into a new 96-well plate. Then, 25 μL of pyruvate solution (150 μL/mL) and 200 μL of β-Nicotinamide adenine dinucleotide (NADH) solution (150 μL/mL), both prepared in 0.1 M phosphate buffer (pH = 7.2) were added. NADH oxidation was monitored at 340 nm. Blank values were subtracted and cytotoxicity was normalized to 100% using Triton X-100 (1%). DMSO (0.5%) was used as solvent control on all assays. All treatments were done in triplicate and in three independent assays, unless otherwise stated. Absorbance was measured using a Cytation 5 Cell Imaging Multi-Mode Reader (BioTek, Vermont,

USA). Cell viability was expressed relative to the solvent control. IC_{50} values were calculated by nonlinear regression model (log(inhibitor) vs. normalized response) on GraphPad Prism 8.4.3.

2.5. Cell viability assays on 3D cell cultures

HCT 116 cells were grown as spheroids using an Ultra-Low Attachment round-bottom 96-well plate (Costar, Corning, New York, NY, USA), at an initial concentration of 5×10^4 cells/mL. After 5 days of incubation, the spheroids were analyzed for size and shape consistency before being randomly exposed to control and to the compounds, at concentrations up to 40 μM. Stauroporine 1 μM was used as positive control and DMSO as solvent control. Viability of HCT 116 spheroids was assessed by the acid phosphatase assay as described by Ferreira et al., 2021 [16].

2.6. Imaging of HCT 116 3D spheroids

At the selected time points after treatment, spheroids were incubated with calcein AM (2 μM) (Invitrogen, Thermo Fisher Scientific) and propidium iodide (5 μg/mL) (Sigma-Aldrich, Missouri, USA) for 1 h. Then, both bright field and fluorescence z-stack images were obtained on a Cytation 5 Cell Imaging Multi-Mode Reader. Fluorescence intensity and morphologic measurements were analyzed using CellProfiler 4.2.8 and ImageJ, respectively. Figures were prepared using Inkscape.

2.7. Quantification of extracellular matrix genes by qPCR

Seven extracellular matrix-related target genes were selected (Table S1). Spheroids treated with phormidolide D (**1**), at 2 and 20 μM for 48 h, were collected and pooled into 8 replicates, each with 8 spheroids. This time point was chosen after optimization of the conditions, since spheroids already present disaggregation without significant cell death (data not shown). RNA was extracted using NucleoSpin RNA XS kit (Macherey-Nagel, Germany), quantified with the Qubit Fluorometer (Invitrogen) and quality assessed by 1% agarose gel electrophoresis. cDNA was synthesized using the iScript Select cDNA Synthesis Kit (BioRad, USA), with 500 ng of RNA reverse-transcribed in a 20 μL reaction. Real-time PCR analysis were performed using the CFX Duet Real-Time PCR System (Bio-Rad). The final reaction volume was 20 μL containing SYBR Green Supermix (Bio-Rad), 200 nM forward and reverse primer, and 2 μL cDNA (1:10 diluted). Reactions were run for 42 cycles of 20s at 95 °C, followed by an annealing temperature of 59 °C and 20 s extension at 72 °C, followed by a melt curve analysis from 65 to 95 °C. The ribosomal protein L8 (*RPL8*) and Hypoxanthine Phosphoribosyl transferase 1 (*HPRT1*) were used as reference genes, as described in a previous work [17], and expression values were normalized to the geometrical mean of both genes. Two negative controls (NTC) were included per gene and run, and all samples were quantified in two independent runs by efficiency-corrected relative expression. The efficiency of each primer was experimentally validated using dose-response curves with serial dilutions of pooled cDNA.

2.8. Combination assay on HCT 116 3D spheroids

HCT 116 spheroids were prepared as described above and exposed for 48 h, alone or in combination with staurosporine, in three independent checkerboard combination assays. Staurosporine was tested at five concentrations (3.13–50 nM) as well as a sub-fraction rich in phormidolide D (**1**) (1.56–25 μg/mL), generating a 5 × 5 dose-response matrix (25 combinations per experiment). The tested fraction is enriched in phormidolide D (**1**), although it also presents phormidolide A (**2**) and other masses as minor components (Fig. S1). Cell viability was assessed by acid phosphatase assay, as described above. The normalized results from the independent assays were submitted into the web-based SynergyFinder platform (synergyfinder.org) [18] for evaluation of drug interactions. A detailed description of the models used to assess synergy scores can be found in the supplementary material.

2.9. Cell cycle, apoptosis and complementary cell death mechanism assays

HCT 116 cells were seeded in 24-well plates at a density of 1 × 105 cells/mL and allowed to adhere overnight. Cells were then treated with compounds (1) and (2) at 0.8 and 8 μM for 48 h. Staurosporine (800 nM) was used as positive control.

For cell cycle analysis, cells were harvested by trypsinization, washed with PBS, fixed in absolute ethanol, and stored at −20 °C. Fixed cells were centrifuged and resuspended in 500 μL of PI/RNase buffer (ABP Biosciences, USA) and incubated for 40 min at 37 °C. Samples were filtered into FACS tubes and analyzed on a BD Accuri C6 Plus flow cytometer (Becton Dickinson, New Jersey, USA). Cells were gated based on forward and side scatter (FSC/SSC) profiles (1st gate: FSC-A/SSC-A, 19–27%, excluding cell debris; 2nd gate: FCS-A/FSC-H: 75–85%, excluding duplets) and analyzed using FlowJo software. At least 10,000 events were acquired per sample.

For apoptosis analysis, cells were collected after treatment, resuspended in Annexin-binding buffer (Invitrogen, Massachusetts, USA) and then stained with FITC Annexin V (5 μL; ImmunoTools, Friesoythe, Germany) and propidium iodide (PI; 10 μL 50 μg/mL) for 15 min in the dark. Samples were filtered into FACS tubes and analyzed on a BD Accuri C6 Plus flow cytometer. At least 10,000 events were acquired per sample, gated using FSC/SSC parameters (1st gate: FSC-A/SSC-A, 35–38%, excluding cell debris; 2nd gate: FCS-A/FSC-H: 99%, excluding duplets) and detected in FL1/FL3 channels. Data were analyzed using FlowJo software.

The autophagy staining with monodansylcadaverine (MDC), glucose-versus-galactose viability assay, mitochondrial membrane potential assay, and temperature-dependent viability assay are described in the Supplementary Information.

2.10. Anti-angiogenesis assay

Embryos of the zebrafish transgenic line Tg(Fli1a:EGFP) were obtained from the animal facility of the Karlsruhe Institute of Technology (KIT). The experimental setup was based on the methodology described in Wang et al., 2010 [19]. At 1-day post fertilization (dpf), chorions were removed by incubation in 1 mg/mL pronase (Roche, Basel, Switzerland) for 15 min, followed by several washes. Dechorionated embryos were exposed to 10 μM of phormidolide D (**1**) in 96-well plates (4 embryos per well). DMSO (0.1%) was used as solvent control. After 24 h of exposure, embryos were individually transferred to 384-well plates and imaged using a LEICA DMi8 (Leica Microsystems, Wetzlar, Germany). Images were analyzed by Image J. Experiments were performed on zebrafish embryos prior to the onset of independent feeding (<5 dpf). According to Directive 2010/63/EU, these developmental stages are not subject to authorization requirements for animal experimentation; therefore, ethical approval was not required.

2.11. Statistical analysis

Statistical analysis was performed using GraphPad 8.4.3 software. Normality of the data was assessed by the Kolmogorov-Smirnov test and, when verified, a One-way ANOVA was applied, followed by Dunnett's multiple comparisons test or Tukey's multiple comparisons test. If data did not obey a normal distribution, a Kruskal-Wallis test was applied, followed by Dunn's post-hoc test. Confidence interval used was 95%, where * means $p < 0.05$; ** means $p < 0.01$; ***means $p < 0.001$, ****means $p < 0.0001$. Cytotoxicity data are presented as mean ± standard deviation (SD) of at least three biological replicates. Dose-response curves were analyzed by log(inhibitor) vs. normalized response using GraphPad software.

3. Results

3.1. Biodiscovery, structural novelty and BGC analysis of phormidolide D (1)

Bioassay-guided fractionation combined with mass spectrometry led to the isolation of the new phormidolide analogue, phormidolide D (**1**), from the crude extract of the marine cyanobacterium *Leptothoe* sp. LEGE 181152. The (−)-HRESIMS spectrum of compound **1** showed a deprotonated molecular ion at *m/z* 1061.5929 $[M-H]^-$ (Fig. S2). The isotopic pattern indicated the presence of one bromine atom, supporting a molecular formula of $C_{58}H_{95}BrO_{12}$ (calcd for $C_{58}H_{94}BrO_{12}$, 1061.5929), corresponding to 11 degrees of unsaturation. Detailed analysis of the 1D and 2D NMR data (Table S2 and Figs. S4-S9), together with (−)-HRESIMS/MS data (Figs. S1 and S2), revealed that **1** is structurally related to the known polyketide phormidolide A (**2**) [10], which was also isolated during the biodiscovery process (Figs. S3 and S10).

Comparison of the ^{1}H and ^{13}C NMR data of phormidolides D (**1**) and A (**2**) (Tables S3 and S4) revealed the most significant differences within the C-30 to C-33 fragment, particularly at C-32 ($\Delta\delta_C = +34.2$ ppm) and C-33 ($\Delta\delta_C = -48.1$ ppm). In phormidolide A (**2**), these carbons form part of a vinyl bromide moiety ($\delta_{C\text{-}32}$ 158.4; $\delta_{C\text{-}33}$ 78.8), whereas in compound **1**, C-32 resonates at δ_C 192.6, consistent with an α,β unsaturated ketone, and C-33 appears as a bromomethylene (δ_C 30.7; δ_H 4.27, 4.18). This structural difference is fully supported by key HMBC correlations from the *exo*-β-methylene protons at δ 6.08 and 5.93 (H-42_a and H42_b) to C-32, as well as from the bromomethylene protons H-33a/b to C-32 (Fig. 2). Together, these data establish the presence of a ketone-bromomethylene motif in phormidolide D (**1**), in place of the methyl-trapped enol ether and vinyl bromide functionality found in phormidolide A (**2**). Further support for this structural modification is provided by the mass difference of 14.01 Da between the two compounds, consistent with a loss of a methyl group in phormidolide D (**1**). This structural modification further distinguishes phormidolide D (**1**) as a new member of the phormidolide family. The relative stereochemistry of **1** was assumed to be identical to that reported for phormidolide A (**2**) [13]. This assignment is supported by key ROESY correlations (Fig. S11) and the close agreement of the proton and carbon chemical shifts of the two compounds (Table S3 and S4).

To investigate the biosynthetic origin of phormidolide D (**1**), the genome of *Leptothoe* sp. LEGE 181152 was analyzed for secondary metabolite biosynthetic genes. This analysis identified two contigs encoding polyketide synthase (PKS) and trans-acyltransferase polyketide synthase (trans-AT PKS) enzymes, which likely correspond to a fragmented phormidolide biosynthetic gene cluster (BGC). Comparison of these contigs with the previously reported *phm* BGC [12] using CAGECAT clinker alignment [20] revealed high synteny (>90% identity and similarity) and extensive conservation of gene content, supporting their assignment as the phormidolide BGC (Fig. S12). These observations however do not allow the prediction of the biosynthetic origin of the bromomethyl ketone of compound 1. Similar results were reported for the related macrolides leptolyngbyalides A and C, produced by *Leptolyngbya* sp. PCC 7375, as the biosynthetic proposed model could not predict the exchange of an enol ether moiety for a methyl ketone [21].

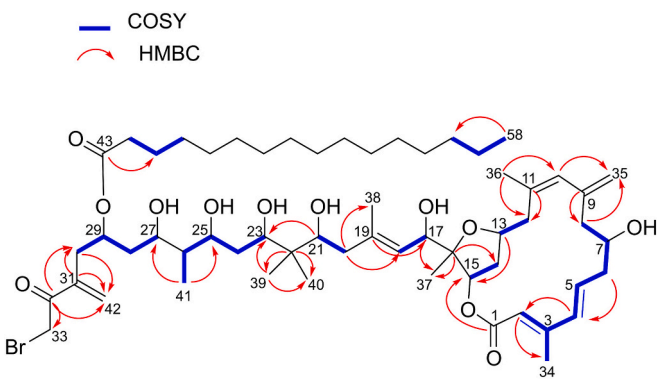


Fig. 2. Structure determination of phormidolide D (**1**). Key $^{1}H—^{1}H$ COSY (bold blue) and $^{13}C—^{1}H$ HMBC (red arrows) correlations supporting the proposed connectivity of the polyketide backbone and macrocyclic structure. (For interpretation of the references to color in this figure legend, the reader is referred to the web version of this article.)

3.2. Phormidolide D (1) exhibits cytotoxicity to 2D and 3D HCT 116 colon carcinoma models, unlike phormidolide A (2)

To characterize the cytotoxic profile of phormidolide D (**1**), the MTT assay was performed after 48 h of exposure on monolayer models of three human cancer cell lines, colorectal carcinoma HCT 116, hepatocellular carcinoma HepG2 and neuroblastoma SH-SY5Y, as well as on the non-cancerous human cerebral microvascular endothelial cell line hCMEC/D3. As demonstrated in Table 1 and Fig. S13, phormidolide D (**1**) exhibited dose-dependent cytotoxicity on all cell lines tested, with IC_{50} values ranging from 0.83 to 4.48 μM. From the three cell lines tested, phormidolide D (**1**) displayed a stronger cytotoxicity towards the HCT 116 cells (Table 1). Additionally, phormidolide D (**1**) reduced the viability of 3D HCT 116 spheroids, presenting an IC_{50} of 30.80 μM, determined by the acid phosphatase assay after 96 h of exposure. The activity observed in both 2D monolayers and 3D spheroid models suggests that the cytotoxic effect of phormidolide D (**1**) is retained in more physiologically relevant cancer models. Given the higher cytotoxicity towards HCT 116 cells, subsequent experiments were focused on this cell line. In comparison, phormidolide A (**2**) showed no cytotoxicity in either model of the colorectal carcinoma cell line HCT 116 at concentrations up to 40 μM (Table 1, Fig. S13), consistent with previous reports [10].

3.3. Phormidolide D (1) alters 3D spheroid morphology and ECM-related gene expression in HCT 116 cells

The morphological changes of HCT 116 spheroids exposed to phormidolides were monitored from 24 h to 96 h at 20 μM (Fig. 3). Throughout this period, phormidolide D (**1**) induced progressive alterations in spheroid morphology, which can be first observed right after 24 h of exposure (1249.51 ± 7.91 μm), and result in an increase in spheroids diameter to 1547.54 ± 41.71 μm at 96 h, nearly doubling the diameter of control (742.72 ± 15.09 μm, 96 h) and compound **2** treated spheroids (756.69 ± 21.42 μm, 96 h). Phormidolide A (**2**) did not induce observable morphological changes relative to the solvent control (Fig. 3A). To further investigate these effects, spheroids were then exposed to 40 μM of phormidolide D (**1**), causing the complete breakdown of the 3D structure, and stained with the live/dead fluorescent dyes calcein AM and propidium iodide (PI) to understand whether the disaggregated cells remained viable. Clear differences were observed between the control (0.5% DMSO) and phormidolide D (**1**) treated spheroids. Control spheroids retained their characteristic layered architecture, including a PI-positive necrotic core and a calcein AM-positive proliferative outer layer. In contrast, spheroids treated with phormidolide D (**1**) showed progressive loss of structural integrity from 24 h onward, with an increasing proportion of detached PI-positive cells over time, as evidenced by intensified PI staining up to the 96 h mark (Fig. 3B). This effect was quantified by an increased PI/Calcein AM fluorescence ratio over 96 h (Fig. 3C). Following the observed morphological alterations, the mRNA expression of seven extracellular matrix (ECM)-related genes was analyzed in spheroids exposed to 20 and 2 μM of compound **1** at the 48 h time point (Fig. 4). At 20 μM, phormidolide D resulted in an 18-fold increase in interstitial collagenase *MMP1* mRNA expression relative to solvent control. In addition, collagen type I *COL1A1* expression was reduced by 2-fold, while the

Table 1
IC_{50} values of phormidolide A (**2**) and of phormidolide D (**1**) in cancerous and non-cancerous cell lines. Data are mean ± SD, from three independent experiments ($n = 3$).

	SH-SY5Y	HepG2	hCMEC/D3	2D HCT 116	3D HCT 116
Phormidolide D (1) IC_{50} (μM)	3.15 ± 0.31	4.48 ± 0.39	2.84 ± 0.53	0.83 ± 0.26	30.80 ± 17.2*
Phormidolide A (2) IC_{50} (μM)	–	–	–	> 50	> 50

* fitted values from the 3D HCT 116 assays: 11.5, 27.6, 53.3 μM.

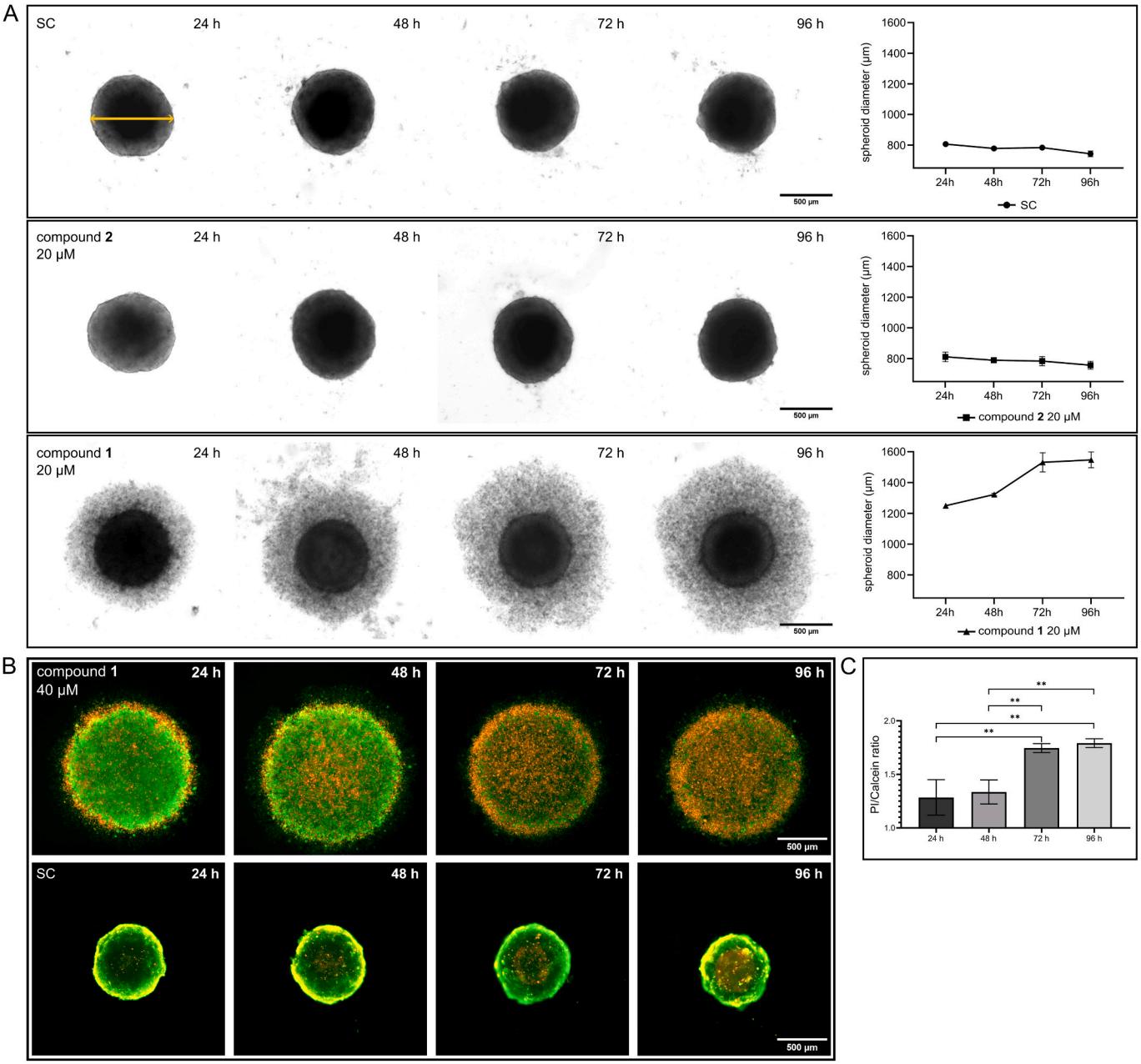


Fig. 3. Effects of phormidolides D (**1**) and A (**2**) on HCT 116 spheroid morphology, size and viability. (A) Bright field images of spheroids exposed to 0.5% DMSO (SC: solvent control); 20 μM compounds **2** and **1** at different time points (24, 48, 72, and 96 h), and corresponding measurements of spheroids diameter (μm). The yellow double arrow represents the diameter measured. (B) Maximum intensity projections of Calcein AM/propidium iodide (PI) fluorescence staining of spheroids at 24, 48, 72 and 96 h exposed to 40 μM phormidolide D (**1**) and 0.5% DMSO (SC). Green fluorescence (calcein AM) indicates viable cells, while orange fluorescence (PI) indicates dead cells. (C) PI/Calcein AM fluorescence intensity ratio in spheroids treated with 40 μM of phormidolide D (1) over 24, 48, 72 and 96 h. Fluorescence quantification was performed using CellProfiler software version 4.2.8. All data are presented as mean ± SD ($n = 3$). (For interpretation of the references to color in this figure legend, the reader is referred to the web version of this article.)

metallopeptidase inhibitor *TIMP1* expression showed a 1.4-fold increase under the same conditions. Although *MMP1* and *TIMP1* were both overexpressed, the fold-change ratio of *MMP1* to *TIMP1* was approximately 12.9, indicating a predominance in *MMP1* expression. The other

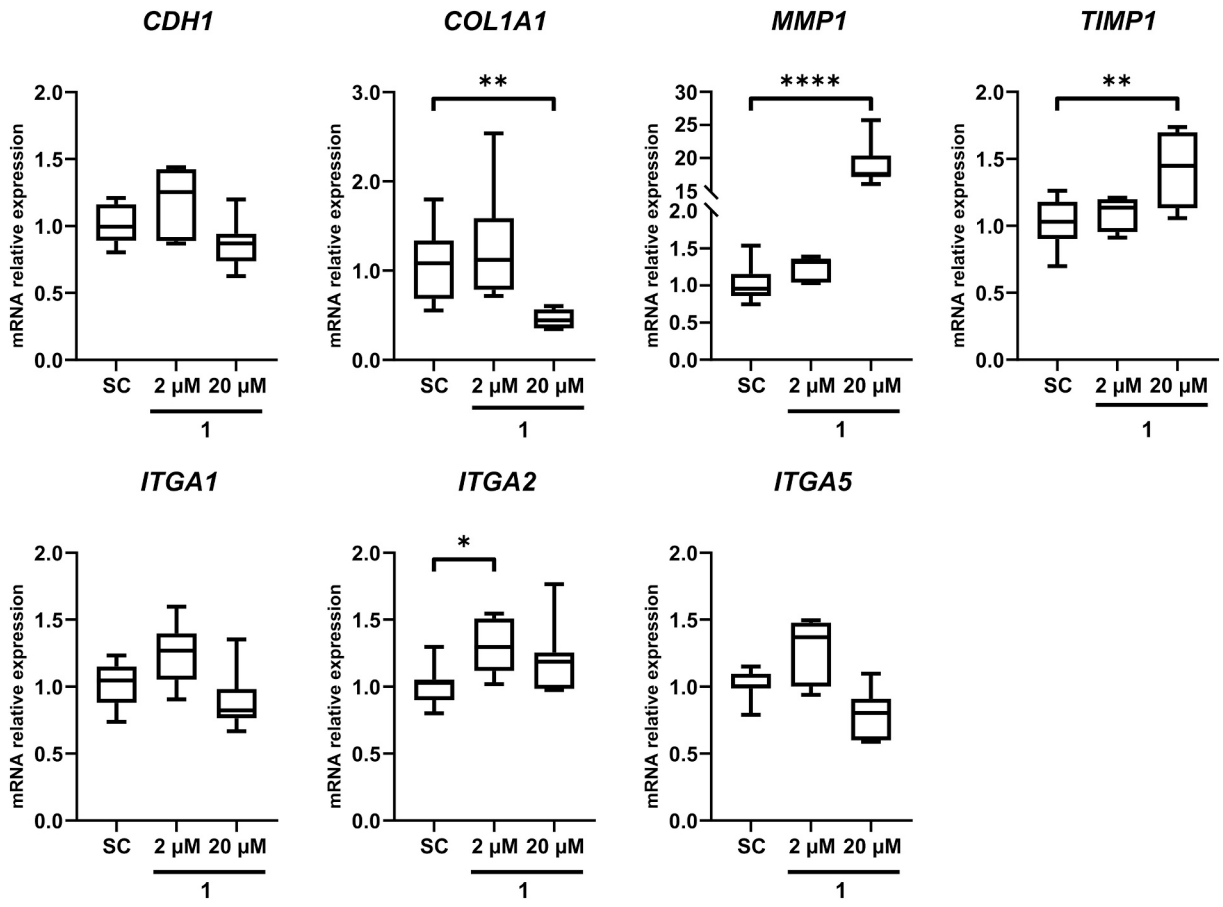


Fig. 4. Relative mRNA expression levels in HCT 116 spheroids exposed for 48 h to 0.5% DMSO (SC - solvent control) and phormidolide D (**1**) at 2 µM and 20 µM. Data represent 8 replicates, with expression values normalized to the geometrical mean of the reference genes *RPL8* and *HPRT1*. Results are shown as box-and-whiskers plots, 5–95 percentile. * $p < 0.05$; ** $p < 0.01$; **** $p < 0.0001$.

analyzed genes, cadherin 1 (*CDH1*), and integrin subunit alpha 1 and alpha 5 (*ITGA 1* and *ITGA5*), showed no significant differences, while integrin subunit alpha 2 *ITGA2* expression was altered at 2 µM, with a 1.3-fold increase.

3.4. Phormidolide D (1) synergizes with staurosporine in HCT 116 spheroids

Based on the observed effects of phormidolide D (**1**) on 3D spheroid integrity, drug-combination experiments were performed using a fraction enriched in phormidolide D (**1**) together with the apoptosis inducer staurosporine at sub-cytotoxic concentrations. Overall, the addition of phormidolide D (**1**) enriched fraction in concentrations ranging from 3.13 to 25 µg/mL, intensified the inhibition caused by staurosporine (Fig. 5A). As seen in Fig. 5B, the addition of the two highest concentrations of each treatment 12.5 and 25 µg/mL (fraction) and staurosporine at 25, 50 nM (staurosporine) yielded the lowest CI values (0.24–0.32), indicating strong synergistic interaction. Similarly, the Bliss synergy model also identified these four combinations as the most synergistic, as demonstrated by their scores exceeding 10, which is representative of a strong synergy (Fig. 5C). The highest score was observed for the combination of 12.5 µg/mL of the phormidolide D-enriched fraction and 25 nM staurosporine at 21.15 (Fig. 5C). Live/dead staining with calcein AM and propidium iodide further highlighted the differences between single-agent and combination treatments. Compared to stausporine alone, combination with phormidolide D (**1**) enriched fraction resulted in increased PI staining and reduced calcein AM fluorescence (Fig. S14). This effect is most evidenced on the combinations with the highest Bliss synergy scores, as shown on Fig. 5D.

3.5. Phormidolide D (1) increases the sub-G1 population and induces early apoptosis without detectable alterations in mitochondrial membrane polarization of HCT 116 cells

Given the pronounced cytotoxicity of phormidolide D (**1**) in HCT 116 cells, its impact on cell cycle progression was investigated by flow cytometry following 48 h of exposure. Treatment with compound **1** resulted in a significant accumulation of cells with reduced DNA stainability, leading to a marked increase in sub-G1 population (48%) compared to the solvent control (SC). This increase was accompanied by a reduction in the G1 and G2 populations (Fig. 6A-B). Similar alterations were observed with the positive control (PC) staurosporine, whereas phormidolide A (**2**) did not induce significant changes in cell cycle distribution. To further characterize the mode of cell death induced by phormidolide D (**1**), apoptosis, necrosis, and autophagy were evaluated. Annexin V/propidium iodide staining revealed a 2.4-fold increase in early apoptotic cells (Q3 - Annexin V-positive/PI-negative) following treatment with compound **1** compared to the solvent control, while no significant changes were observed for any other quartile or in cells treated with compound **2** (Fig. 6C-D). Consistently, the LDH release assay confirmed that compound **1** does not predominantly induce cell death via necrosis. At the highest concentration tested, LDH release reached only approximately 20% relative to the maximum release induced by 1% Triton X-100, and all treated conditions were significantly different from this positive control (Fig. S15). Autophagy was evaluated using monodansylcadaverine staining, which showed no detectable differences between control and phormidolide D (**1**) treated cells, suggesting that autophagy is not a primary mechanism of cell death (Fig. S16).

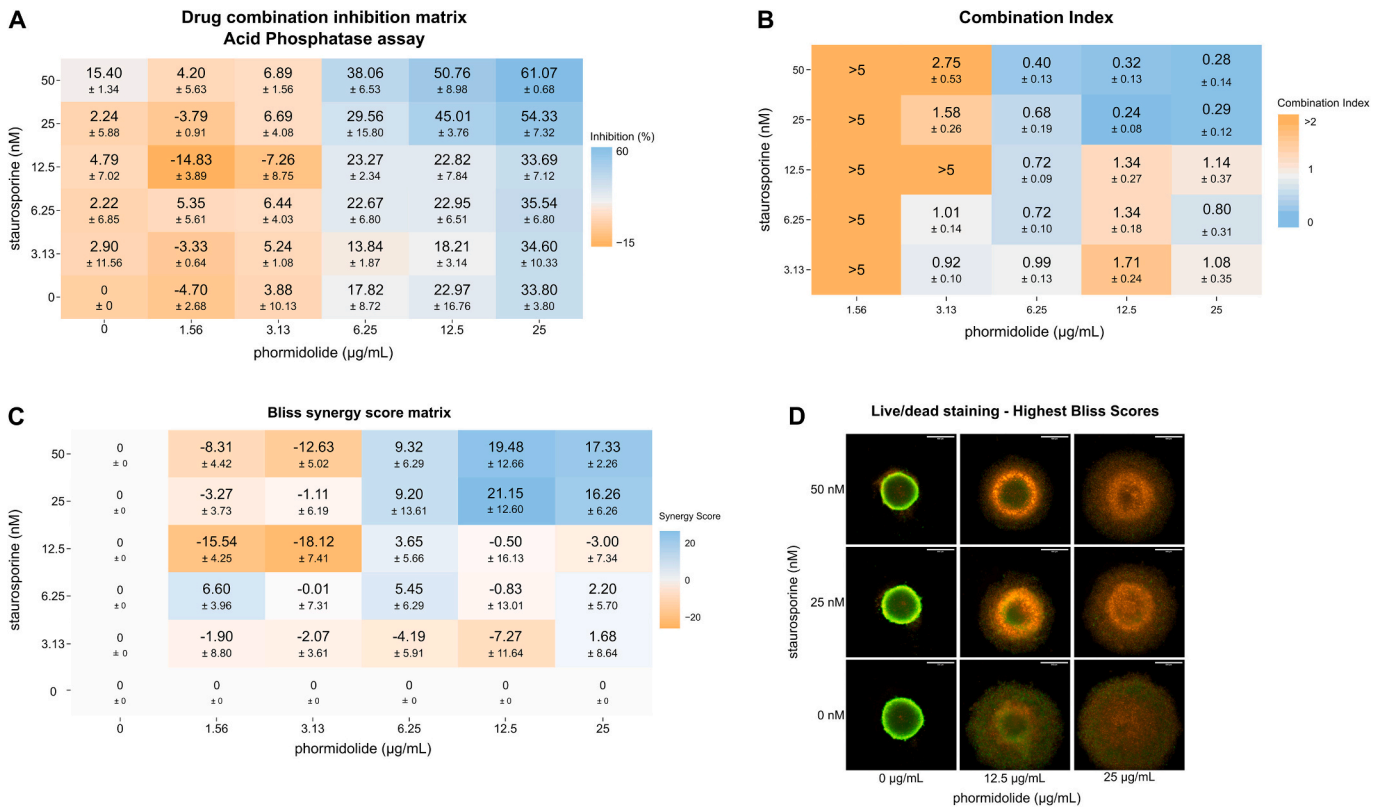


Fig. 5. Combination effects of phormidolide D (**1**)-enriched fraction and staurosporine in HCT116 spheroids. (A) Heatmap representing the dose-response matrix of the combination of a phormidolide D (**1**)-enriched fraction (x axis, µg/mL) and staurosporine (y axis, nM). Color scale represents the percentage of inhibition of cell viability plus standard deviation. (B) Heatmap of the combination index values (top value) plus standard deviation. Color scale represents the magnitude of the index value, with values below 1 in blue representing synergy, while higher values (orange) represent antagonism. (C) Bliss synergy score heatmap, and its standard deviation (bottom value). Color scale represents the magnitude of the score, with positive values in blue representing synergy while negative values (orange) represent antagonism. (D) Representative live/dead staining of HCT116 spheroids treated with the most synergistic combinations of the phormidolide D (**1**)-enriched fraction and staurosporine, together with the corresponding single-agent treatments. Data from three independent assays, $n = 3$. (For interpretation of the references to color in this figure legend, the reader is referred to the web version of this article.)

To further characterize the cytotoxic mechanism of phormidolide D (**1**), complementary assays evaluating oxidative phosphorylation dependence, mitochondrial membrane potential, and temperature-dependent cytotoxicity were performed. The IC_{50} values obtained in glucose (0.87 µM ± 0.46) or galactose (0.97 µM ± 0.41) media did not show any significant differences (Fig. S17). Likewise, no alterations in mitochondrial membrane polarization were detected in cells treated with phormidolide D (**1**) at IC_{50} and 2xIC_{50} concentrations (Fig. S18). Finally, cells incubated with phormidolide D (**1**) for 1 h at 4 °C exhibited a fivefold higher IC_{50} (14.79 µM ± 6.93) than those incubated at 37 °C (2.77 µM ± 0.64) (Fig. S19), indicating that the cytotoxic activity of phormidolide D (1) is temperature dependent.

3.6. *Phormidolide D (1) affects vascularization of zebrafish embryos*

The anti-angiogenic activity of phormidolide D (**1**) was evaluated using embryos of the transgenic zebrafish line Tg(*fli1a*:EGFP), which enables direct visualization of the vasculature, particularly intersegmental vessels (ISV) (Fig. S20). Exposure to 10 µM phormidolide D (**1**) for 48 h did not affect embryo width (Fig. 7A), nor induced malformations or toxicity (data not shown). Phormidolide D (**1**) significantly reduced both the number and length of ISVs (Fig. 7B – C, Fig. S20), suggesting a possible anti-angiogenic activity. However, this activity should be corroborated by more concentrations and higher replicate numbers in the future.

4. Discussion

Cyanobacteria of the genus *Leptothoe* are marine strains, some of which occur as sponge symbionts, and represent a rich source of structurally diverse secondary metabolites [22]. In this context, *Leptothoe* sp. LEGE 181152, a free-living isolate collected in Cabo Verde, has emerged as a chemically rich strain, producing metabolites with diverse biological activities, including antifouling compounds [23] and the leptochelins, halogenated nonribosomal peptide–polyketide hybrids with cytotoxic and metallophore properties [11]. Building on this biosynthetic potential, we report herein the discovery of phormidolide D (**1**), a new polyketide of the phormidolide family featuring a rare modification of the canonical vinyl bromide moiety into a conjugated ketone–bromomethyl system. This distinct terminal functionalization, which differentiates phormidolide D (**1**) from the known congener phormidolide A (**2**), enabled direct structure–activity comparisons for investigating the determinants of cytotoxic activity within this scaffold.

Phormidolide D (**1**) exhibited cytotoxicity (< 5 µM) across all cell lines evaluated, and higher potency against HCT 116 colorectal carcinoma cells (0.83 µM). Phormidolide A (**2**) was inactive, consistent with the previously reported lack of cytotoxicity for this analogue [10]. The contrasting activity between the two closely related compounds suggests that the bromomethylene-containing terminal motif is an important structural determinant associated with cytotoxic activity of phormidolide D (**1**).

A major challenge in anticancer natural product discovery is the limited predictive value of conventional two-dimensional (2D) cell

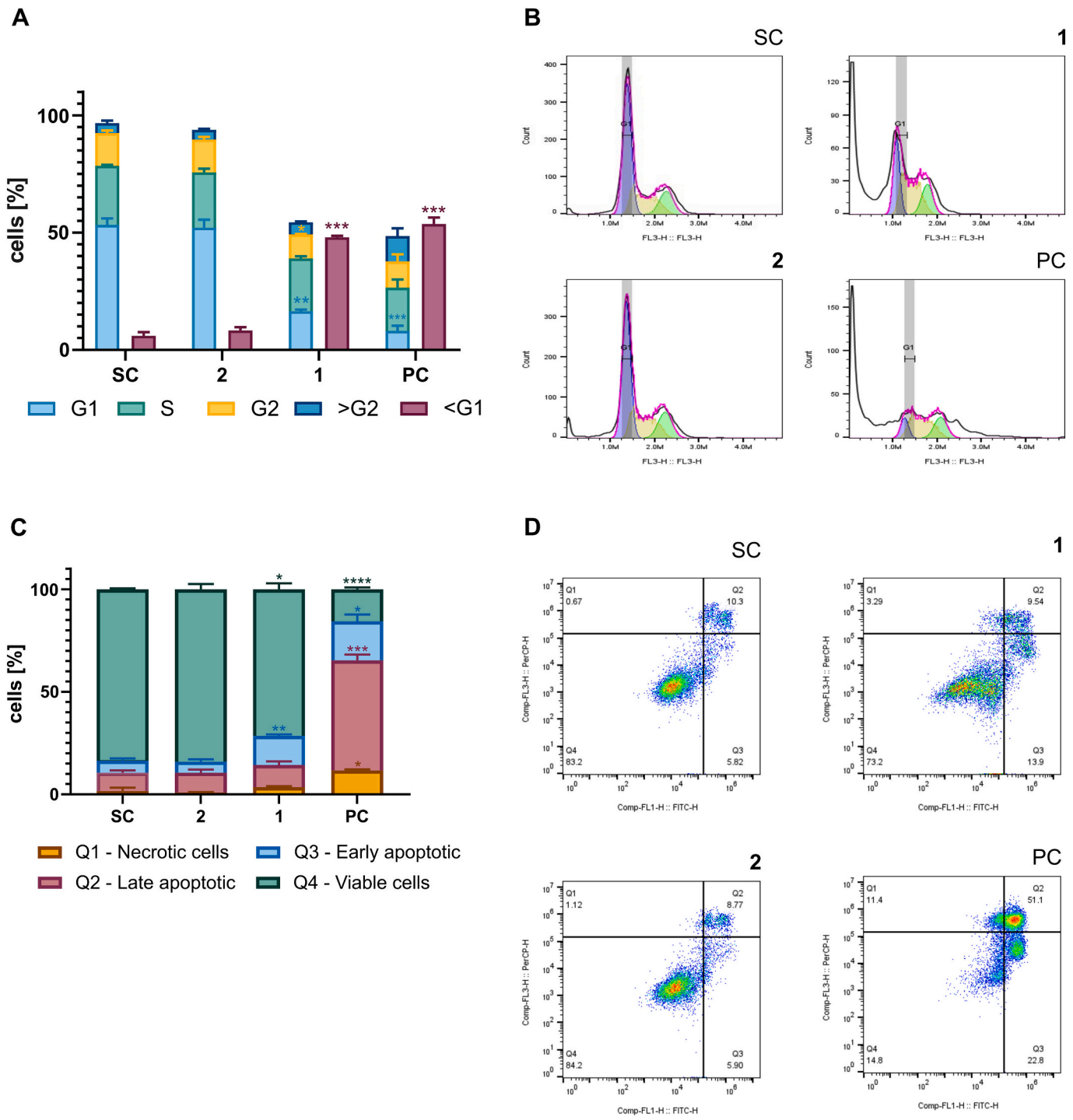


Fig. 6. Effects of phormidolide D (**1**) on the cell cycle and apoptosis in HCT 116 cells. (A) Quantification of cell cycle phase distribution showing accumulation of the sub-G1 population in cells treated with phormidolide D (**1**). (B) Representative histograms of cell cycle analysis by flow cytometry. (C) Quantification of apoptotic cell populations after Annexin V/propidium iodide staining. (D) Representative flow cytometry quadrant plots showing viable cells (Q4), early apoptotic cells (Q3), late apoptotic cells (Q2), and necrotic cells (Q1). Cells were exposed for 48 h to: SC - solvent control 0.5% DMSO, **1**–8 μM phormidolide D; **2**–8 μM phormidolide A (**2**), and PC - positive control 800 nM staurosporine. Data represent mean ± SD ($n = 3$). * $p < 0.05$, ** $p < 0.01$; *** $p < 0.001$, **** $p < 0.0001$.

cultures, which fail to reproduce many characteristics of solid tumors in vivo [24]. Three-dimensional (3D) spheroid cultures have therefore emerged as more physiologically relevant systems, as they better reproduce key features of the tumor microenvironment, including cell–cell and cell–ECM interactions, as well as nutrients and oxygen gradients [25]. When evaluated in the HCT 116 3D spheroid model, phormidolide D (**1**) retained cytotoxic activity under more physiologically relevant conditions, albeit with reduced potency compared to monolayer cultures. This decrease in potency is consistent with reports for other cytotoxic agents and reflects the increased drug resistance and structural complexity characteristic of multicellular tumor models [24]. Phormidolide D (**1**)-treated spheroids displayed a marked phenotypic effect: an increase in spheroid diameter followed by progressive shedding of cells from the spheroid surface. Live/dead (Calcein AM/PI) staining demonstrated that these detached cells were predominantly non-viable, indicating that the increase in spheroid size reflected cell

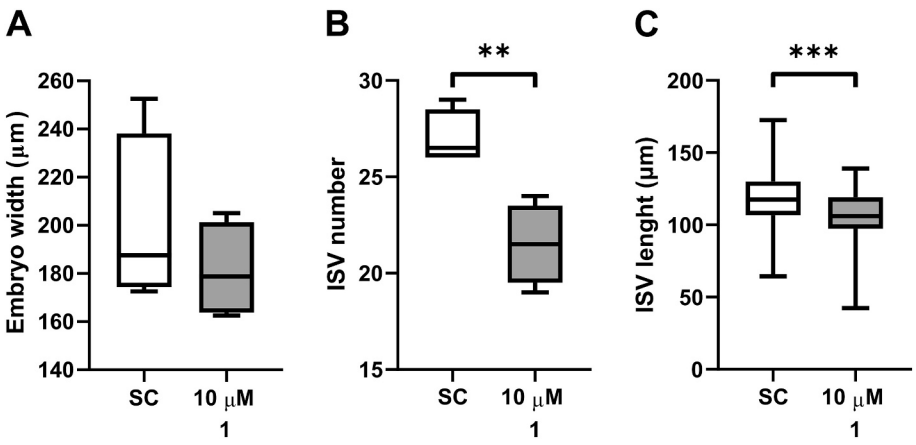


Fig. 7. Reduction of vascularization by phormidolide D (**1**) in embryos of the zebrafish lineTg(*fli1a*:EGFP). Embryo width (A), intersegmental vessels (ISV) number (B) and ISV length (C) were measured in embryos exposed for 24 h to 0.1% DMSO (SC, solvent control) and to 10 µM phormidolide D (**1**). Four individual embryos were analyzed per condition. Data are represented as box-and-whisker plots (5th–95th percentiles). Asterisks indicate statistically significant differences (** $p < 0.01$; *** $p < 0.001$, unpaired *t*-test).

death and loss of structural cohesion rather than enhanced proliferation. Similar phenotypes have been reported for paclitaxel and doxorubicin in other spheroid models, where spheroid disaggregation and altered morphology have been associated with ECM remodeling [26], [27]. In contrast, phormidolide A (**2**) did not induce any morphological changes, reinforcing the proposed role of the bromomethylene-containing terminal motif in the observed effects. Given the role of ECM in maintaining spheroid cohesion, this phenotype was further investigated at the molecular level through analysis of the relative mRNA expression of ECM-related genes. Of the seven tested genes, only *MMP1*, *COL1A1* and *TIMP1* presented relevant alterations of their expression levels. Phormidolide D (**1**) treatment decreased expression of type I collagen, a structural ECM component that has been linked to tumorigenesis by contributing to tumor rigidity, limiting drug penetration and reducing therapeutic efficacy [28]. Consistently, treatment was associated with a pronounced increase in the matrix metallopeptidases *MMP1*, a key mediator of ECM degradation and particularly of collagens [29]. Together, these findings indicate a putative ECM remodeling induced by phormidolide D (**1**), consistent with the observed morphological alterations of the spheroid architecture. Future work should extend to verify the ECM remodeling effect by analyzing protein level or functional evidence at different time points.

Given that drug diffusion and therapeutic outcomes within solid tumors are strongly influenced by ECM integrity [30], we hypothesized that phormidolide D (**1**) could enhance the efficacy of combination treatments. To test this, a fraction enriched in compound **1** was tested in combination with sub-toxic doses of staurosporine, which showed an overall increase in staurosporine activity, where four combinations yielded synergy scores above 10, indicative of a strong synergism. The stronger score was observed on the combination of 12.5 µg/mL of the phormidolide D (**1**) fraction and 25 nM of staurosporine, which also presented the lowest combination index value of 0.24. In this combination, the interaction of both treatments augmented the inhibition by 2 and 20-fold in relation to the activity observed on phormidolide D (**1**) fraction and staurosporine alone, respectively. These results support that the phormidolide D (**1**) enriched fraction and enhances the activity of staurosporine, potentially by targeting the 3D spheroid architecture and increasing drug penetration within the tumor-like structure, thereby enabling biological effects at lower doses. Collectively, these findings support further investigation of phormidolide D (**1**) in combination therapy strategies for solid tumors.

Next, we sought to determine the specific mechanism of cell death underlying these effects, given that understanding such mechanisms is of primary importance for characterizing compound activity and supporting lead development in cancer drug discovery. Cell cycle distribution and apoptotic pathways were therefore evaluated. An accumulation of cells in the sub-G1 region, indicative of DNA fragmentation, was observed in the phormidolide D (**1**) group, as well as in the positive control staurosporine. This is typically considered a hallmark of apoptosis but may also arise from necrotic processes leading to DNA degradation [31]. Annexin V/PI staining showed a small, but significant increase in cells in early apoptosis without significant changes in late apoptosis or necrosis. The limited LDH release further argues against necrotic cell death, while monodansylcadaverine staining did not support the involvement of autophagy. Collectively, these findings indicate that phormidolide D (**1**) induces apoptotic cell death, with no evidence for a major contribution of necrosis or autophagy. To investigate whether this cytotoxic activity was associated with mitochondrial dysfunction, mitochondrial metabolic dependence and function were assessed using complementary approaches. The glucose/galactose assay, which forces cells to rely predominantly on oxidative phosphorylation [32], showed no significant differences between the different culture media, suggesting that the cytotoxic effects of phormidolide D (**1**) are not associated with mitochondria dysfunction. Consistently, staining with tetramethylrhodamine (TMRM) did not reveal any alterations in mitochondria membrane potential. Together, these findings indicate that phormidolide D (**1**) does not directly impair mitochondrial metabolism.

As drug uptake and intracellular trafficking are generally reduced at low temperature, cytotoxicity was also evaluated following incubation at 4 °C. Although phormidolide D (**1**) retained measurable cytotoxic activity under these conditions ($IC_{50} = 14$ µM), its potency was reduced approximately fivefold compared with cells incubated at 37 °C. These findings indicate that the cytotoxic activity is influenced by temperature-sensitive cellular processes, although whether this reflects altered cellular uptake, membrane dynamics, or other temperature-dependent mechanisms remains to be determined.

In addition to these in vitro models, the anti-angiogenic potential of phormidolide D (**1**) was evaluated in vivo using zebrafish embryos. Zebrafish have become a widely used vertebrate model in drug discovery for studying human diseases, including cancer, due to their high genetic homology with human genes associated with diseases, and their suitability for genetic manipulation [33]. The transgenic Tg(*fli1a*:EGFP) line used in this study expresses enhanced green fluorescence protein in endothelial cells, allowing the direct visualization of vasculature, providing a robust model for evaluating anti-angiogenic activity [34].

Exposure to phormidolide D (**1**) reduced the formation of intersegmental vessels without the induction of any malformations or toxicity,

indicating a possible in vivo anti-angiogenic effect, which should be corroborated in the future.

5. Conclusions

In this work, we report the isolation and structural and biological characterization of phormidolide D (**1**), a novel cytotoxic member of the phormidolide family, alongside the known analogue phormidolide A (**2**), from the marine cyanobacterium *Leptothoe* sp. LEGE 181152. This discovery further highlights the remarkable biosynthetic capacity of this strain, previously recognized as a source of cytotoxic metallophores and antifouling metabolites. Although phormidolides A (**2**) and D (**1**) share the same macrolide scaffold, their markedly different biological activities suggest that the bromomethylene ketone moiety in phormidolide D (**1**) is a key structural determinant of its cytotoxic activity. Beyond its potent cytotoxicity, phormidolide D (**1**) affected the extracellular matrix of cancer spheroids, enhanced the activity of a cytotoxic drug in combination assays, and reduced the vascularization of zebrafish embryos, warranting further studies for its anti-angiogenic potential. Together, these findings provide new insights into the structure–activity relationships within the phormidolide family and identify phormidolide D (**1**) as a promising marine natural product lead for anticancer drug discovery. Future studies should focus on identifying its molecular target, defining its mechanism of action, and evaluating its therapeutic potential in combination strategies.

CRediT authorship contribution statement

Leonor Ferreira: Writing – original draft, Methodology, Investigation, Formal analysis. **Tiago Ribeiro:** Writing – original draft, Investigation. **Ravindra Peravali:** Writing – review & editing, Resources, Methodology, Funding acquisition. **Vítor Vasconcelos:** Writing – review & editing, Funding acquisition. **Ralph Urbatzka:** Writing – review & editing, Supervision, Funding acquisition, Formal analysis, Conceptualization. **Mariana Reis:** Writing – review & editing, Writing – original draft, Supervision, Funding acquisition, Conceptualization.

Funding

This work was supported by the project CyanoMetAl – Discovery of Cyanobacterial Metal-Chelating Agents: A Multifunctional Solution for Alzheimer's Disease (COMPETE2030-FEDER-00876800), funded by the European Regional Development Fund (ERDF/FEDER) under the Innovation and Digital Transition Thematic Programme (COMPETE 2030), and by national funds through FCT – Fundação para a Ciência e a Tecnologia under the projects UID/04423/2025 (https://doi.org/10.54499/UID/04423/2025), UID/PRR/04423/2025 (https://doi.org/10.54499/UID/PRR/04423/2025), and LA/P/0101/2020 (https://doi.org/10.54499/LA/P/0101/2020) and by the WP9- Portuguese Blue Biobank under the Blue Economy Pact - Project N°. C644915664–00000026 co-funded by PRR, The Portuguese Republic and the European Union.

Leonor Ferreira is supported by Fundação para a Ciência e a Tecnologia (FCT) PhD Grant with the reference 2022.11979.BD, https://doi.org/10.54499/2022.11979.BD.

Declaration of competing interest

The authors declare the following financial interests/personal relationships which may be considered as potential competing interests: Mariana Reis has patent #EP4233857 issued to no licensee. Leonor Ferreira has patent #EP4233857 issued to no licensee. Vitor Vasconcelos has patent #EP4233857 issued to no licensee. If there are other authors, they declare that they have no known competing financial interests or personal relationships that could have appeared to influence the work reported in this paper.

Appendix A. Supplementary data

Supplementary data to this article can be found online at https://doi.org/10.1016/j.bioorg.2026.110637.

Data availability

The NMR data for phormidolides have been deposited in NP-MRD; www.np-mrd.org at NP0352096(phormidolide D). HRESIMS/MS spectra of phormidolide A and D is available in MassIVE (MSV000100394).

References

[1] P. Piña-Sánchez, et al., Cancer biology, epidemiology, and treatment in the 21st century: current status and future challenges from a biomedical perspective, Cancer Control 28 (2021) 10732748211038735, https://doi.org/10.1177/10732748211038735.
[2] F. Bray, et al., Global cancer statistics 2022: GLOBOCAN estimates of incidence and mortality worldwide for 36 cancers in 185 countries, *CA Cancer J. Clin.* 74 (3) (2024), https://doi.org/10.3322/caac.21834.
[3] J.J. Lee, K.Y. Ng, A. Bakhtiar, Extracellular matrix: unlocking new avenues in cancer treatment, Biomark. Res. 13 (1) (2025) 78, https://doi.org/10.1186/s40364-025-00757-3.
[4] N.K. Karamanos, et al., A guide to the composition and functions of the extracellular matrix, FEBS J. 288 (24) (2021) 6850–6912, https://doi.org/10.1111/febs.15776.
[5] J.R. Libby, H. Royce, S.R. Walker, L. Li, The role of extracellular matrix in angiogenesis: beyond adhesion and structure, Biomater. Biosyst. 15 (2024) 100097, https://doi.org/10.1016/j.bbiosy.2024.100097.
[6] Z.-L. Liu, H.-H. Chen, L.-L. Zheng, L.-P. Sun, L. Shi, Angiogenic signaling pathways and anti-angiogenic therapy for cancer, Signal Transduct. Target. Ther. 8 (1) (2023) 198, https://doi.org/10.1038/s41392-023-01460-1.
[7] D.J. Newman, G.M. Cragg, Natural products as sources of new drugs over the nearly four decades from 01/1981 to 09/2019, J. Nat. Prod. 83 (3) (2020) 770–803, https://doi.org/10.1021/acs.jnatprod.9b01285.
[8] L.N. Aldrich, et al., Discovery of anticancer agents of diverse natural origin, J. Nat. Prod. 85 (3) (2022) 702–719, https://doi.org/10.1021/acs.jnatprod.2c00036.
[9] H. Luesch, E.K. Ellis, Q.-Y. Chen, R. Ratnayake, Progress in the discovery and development of anticancer agents from marine cyanobacteria, Nat. Prod. Rep. 42 (2) (2025), https://doi.org/10.1039/D4NP00019F.
[10] R.T. Williamson, A. Boulanger, A. Vulpanovici, M.A. Roberts, W.H. Gerwick, Structure and absolute stereochemistry of Phormidolide, a new toxic metabolite from the marine cyanobacterium Phormidium sp, J. Organomet. Chem. 67 (23) (2002) 7927–7936, https://doi.org/10.1021/jo020240s.
[11] N.E. Avalon, et al., Leptochelins A–C, cytotoxic metallophores produced by geographically dispersed *Leptothoe* strains of marine cyanobacteria, J. Am. Chem. Soc. 146 (27) (2024), https://doi.org/10.1021/jacs.4c05399.
[12] M.J. Bertin, et al., The Phormidolide biosynthetic gene cluster: a *trans* -AT PKS pathway encoding a toxic macrocyclic polyketide, ChemBioChem 17 (2) (2016) 164–173, https://doi.org/10.1002/cbic.201500467.
[13] I.E. Ndukwe, et al., Synergism of anisotropic and computational NMR methods reveals the likely configuration of phormidolide a, Chem. Commun. 56 (55) (2020), https://doi.org/10.1039/D0CC03055D.
[14] A. Lorente, A. Gil, R. Fernández, C. Cuevas, F. Albericio, M. Álvarez, Phormidolides B and C, cytotoxic agents from the sea: enantioselective synthesis of the macrocyclic core, Chem. Eur. J. 21 (1) (2015), https://doi.org/10.1002/chem.201404341.
[15] G. Muir, I. Paterson, N.Y.S. Lam, R. Britton, Synthesis of the Phormidolide a macrocycle supports the proposed configurational reassignment, Org. Lett. 26 (40) (2024) 8548–8553, https://doi.org/10.1021/acs.orglett.4c03171.
[16] L. Ferreira, et al., Uncovering the bioactive potential of a cyanobacterial natural products library aided by untargeted metabolomics, Drugs 19 (11) (2021), https://doi.org/10.3390/md19110633.
[17] S. Freitas, et al., Insights into the potential of picoplanktonic marine cyanobacteria strains for cancer therapies – cytotoxic mechanisms against the RKO colon cancer cell line, Toxicon 119 (2016) 140–151, https://doi.org/10.1016/j.toxicon.2016.05.016.
[18] S. Zheng, et al., SynergyFinder plus: toward better interpretation and annotation of drug combination screening datasets, Genomics Proteomics Bioinformatics 20 (3) (2022) 587–596, https://doi.org/10.1016/j.gpb.2022.01.004.
[19] C. Wang, et al., Rosuvastatin, identified from a zebrafish chemical genetic screen for antiangiogenic compounds, suppresses the growth of prostate Cancer, Eur. Urol. 58 (3) (2010) 418–426, https://doi.org/10.1016/j.eururo.2010.05.024.
[20] C.L.M. Gilchrist, Y.-H. Chooi, Clinker & clustermap.Js: automatic generation of gene cluster comparison figures, Bioinformatics 37 (16) (2021) 2473–2475, https://doi.org/10.1093/bioinformatics/btab007.
[21] E.J.N. Helfrich, et al., Automated structure prediction of trans-acyltransferase polyketide synthase products, Nat. Chem. Biol. 15 (8) (2019) 813–821, https://doi.org/10.1038/s41589-019-0313-7.

[22] D. Konstantinou, R.V. Popin, D.P. Fewer, K. Sivonen, S. Gkelis, Genome reduction and secondary metabolism of the marine sponge-associated cyanobacterium *Leptothoe*, Drugs 19 (6) (2021) 298, https://doi.org/10.3390/md19060298.
[23] S. Pereira, et al., Bioassay-guided discovery of antifouling nucleosides from the cyanobacterium Leptothoe sp. LEGE 181152: efficacy, molecular targets, and ecotoxicological assessment, Ecotoxicol. Environ. Saf. 305 (2025) 119175, https://doi.org/10.1016/j.ecoenv.2025.119175.
[24] N. Kaur, et al., Navigating Cancer treatment: a journey from 2D to 3D Cancer models and nanoscale therapies, ACS Pharmacol. Transl. Sci. 8 (11) (2025) 3773–3800, https://doi.org/10.1021/acsptsci.5c00530.
[25] M.A.G. Barbosa, C.P.R. Xavier, R.F. Pereira, V. Petrikaitė, M.H. Vasconcelos, 3D cell culture models as recapitulators of the tumor microenvironment for the screening of anti-cancer drugs, Cancers 14 (1) (2021), https://doi.org/10.3390/cancers14010190.
[26] N. Baek, O.W. Seo, M. Kim, J. Hulme, S.S.A. An, Monitoring the effects of doxorubicin on 3D-spheroid tumor cells in real-time, Onco. Targets Ther. Volume 9 (2016) 7207–7218, https://doi.org/10.2147/OTT.S112566.
[27] J. Culley, P.W. Nagle, J.C. Dawson, N.O. Carragher, Patient derived glioma stem cell spheroid reporter assays for live cell high content analysis, SLAS Discov. 28 (2) (2023) 13–19, https://doi.org/10.1016/j.slasd.2022.09.002.
[28] Y. Song, S. Kim, K.M. Kim, E.K. Choi, J. Kim, H.R. Seo, Activated hepatic stellate cells play pivotal roles in hepatocellular carcinoma cell chemoresistance and migration in multicellular tumor spheroids, Sci. Rep. 6 (1) (2016) 36750, https://doi.org/10.1038/srep36750.
[29] S. Mustafa, S. Koran, L. AlOmair, Insights into the role of matrix metalloproteinases in Cancer and its various therapeutic aspects: a review, Front. Mol. Biosci. 9 (2022) 896099, https://doi.org/10.3389/fmolb.2022.896099.
[30] E. Henke, R. Nandigama, S. Ergün, Extracellular matrix in the tumor microenvironment and its impact on cancer therapy, Front. Mol. Biosci. 6 (2020) 160, https://doi.org/10.3389/fmolb.2019.00160.
[31] C. Riccardi, I. Nicoletti, Analysis of apoptosis by propidium iodide staining and flow cytometry, Nat. Protoc. 1 (3) (2006) 1458–1461, https://doi.org/10.1038/nprot.2006.238.
[32] M.L. Sousa, M. Preto, V. Vasconcelos, S. Linder, R. Urbatzka, Antiproliferative effects of the natural oxadiazine nocuolin a are associated with impairment of mitochondrial oxidative phosphorylation, Front. Oncol. 9 (APR) (2019), https://doi.org/10.3389/fonc.2019.00224.
[33] C. Liu, et al., Recent advances of the zebrafish model in the discovery of marine bioactive molecules, Drugs 22 (12) (2024) 540, https://doi.org/10.3390/md22120540.
[34] N.D. Lawson, B.M. Weinstein, In vivo imaging of embryonic vascular development using transgenic zebrafish, Dev. Biol. 248 (2) (2002) 307–318, https://doi.org/10.1006/dbio.2002.0711.